Rapid 3D whole-heart cine imaging using golden ratio stack of spirals

Javier Montalt-Tordera[1], Grzegorz Kowalik[1], Alexander Gotschy[2,3], Jennifer Steeden[1], Vivek Muthurangu[1]

[1] *UCL Institute of Cardiovascular Science, UCL, London, UK*
[2] *Great Ormond Street Hospital, London, UK*
[3] *Institute for Biomedical Engineering, University and ETH Zurich, Zurich, Switzerland*

All correspondence should be addressed to Javier Montalt-Tordera (*javier.tordera.17@ucl.ac.uk*).

E-mail address for rest of authors:

Grzegorz Kowalik: *grzegorz.kowalik.09@ucl.ac.uk*
Alexander Gotschy: *Alexander.Gotschy@usz.ch*
Jennifer Steeden: *jennifer.steeden@ucl.ac.uk*
Vivek Muthurangu: *v.muthurangu@ucl.ac.uk*

spacing in k_z, between consecutive readouts. This is unsuitable for bSSFP sequences, which exhibit image artefacts when subject to large stepwise changes in eddy currents [17]. Therefore, alternative sampling strategies must be considered to adapt GRASS for use in a bSSFP pulse sequence, such as uniform and tiny golden ratio [18] sampling.

This work presents a rapid free-breathing whole-heart cine imaging framework based on a stack of spirals trajectory with a parallel imaging and compressed sensing reconstruction. The aims were to: (1) investigate the optimal ordering scheme for a stack of spirals cine sequence using an *in silico* model, (2) implement such a sequence and test it *in vivo* and (3) evaluate image quality and quantitative measurements against the gold standard examination, i.e. 2D multi-slice breath-hold imaging.

2 MATERIALS AND METHODS

This work is divided into two parts: (1) a simulation study comparing two different step sizes in k_z, and (2) a patient study comparing the resulting technique to conventional 2D multi-slice breath-hold imaging.

2.1 Sequence Design

The sequence employed in this work is a 3D bSSFP stack of spirals acquired in a transverse orientation. A uniform density spiral trajectory was designed using the method described by Pipe et al. [19], assuming a field-of-view of 450 mm, a spatial resolution of 2.0 × 2.0 mm and 90 uniformly spaced spiral arms for complete filling of *k*-space, at each of the 104 k_z partitions.

A golden ratio stack of spirals (GRASS) sampling strategy was used [15], which is based on a continuously running nested loop strategy. In the inner loop, consecutive spiral interleaves were advanced in the k_z direction, while keeping their k_x-k_y position the same. Each inner loop consisted of 104 steps and was followed by an outer loop rotation of the spiral arm by the golden angle (~222°) [20] (Figure 1).

The following imaging parameters were used: TR/TE = 3.42/0.95 ms, FOV = 450 × 450 × 210 mm^3, matrix size = 224 × 224 × 104, voxel size = 2.0 × 2.0 × 2.0 mm^3, flip angle = 60°, bandwidth = 1,590 Hz/pixel. A total of 62,400 readouts were continuously acquired for a fixed scan time of 3 min 33 s.

When using non-Cartesian trajectories such as spirals, some attention must be dedicated to ensuring trajectory fidelity. In modern scanners, the most important source of trajectory errors is the gradient delay relative to the ADC. This can be easily adjusted by appropriately shifting the ADC window and/or correcting the trajectory. The delay is typically different for each

physical gradient axis [21]. However, if these differences are relatively small, as is the case for the scanner used in this work, using a single optimized delay affords most of the benefit while simplifying the implementation [22]. In the present work, the delay was set to the average of the delays in the *x* and *y* physical axes (ignoring *z* as it was only used for phase encoding).

2.2 Reconstruction

The same reconstruction was used for both the simulation and patient studies. We expanded on the previously described GRASS framework [15], to develop XD-GRASS which sorts the data into cardiac and respiratory motion states, and reconstructs the undersampled multidimensional dataset using parallel imaging and compressed sensing, similar to [8]. This method has the advantage of exploiting sparsity in the respiratory dimension.

Data were retrospectively gated into 20 cardiac phases and 4 respiratory phases, totalling 80 volumes, with an acceleration factor of ~12. Cardiac gating was based on timestamps (provided from the vector cardiogram signal in the patient study, simulated timestamps in the simulation study). In order to obtain respiratory information, head-foot projections were retrospectively extracted from the *k*-space samples in the k_z axis, both in the patient study and the simulation study (Figure 2). This has been previously described for stack of spirals data and validated against respiratory bellows [15]. A method based on principal component analysis (PCA) and Fourier analysis was then used to extract a respiratory signal from the projections [23]. Such a signal has been shown to be a reliable indicator of respiratory position. Finally, the respiratory signal was used to sort the *k*-space samples into respiratory bins from end-expiration to end-inspiration [16].

After data sorting, an iterative reconstruction combining parallel imaging and compressed sensing was used to obtain images from a subsampled *k*-space. Prior to the reconstruction, coil compression was performed in order to limit computational cost [24]. Then, coil sensitivity maps were obtained for the virtual coils using the ESPIRiT method [25].

After calibration, images m were reconstructed from sorted *k*-space data d by solving the following optimization problem [16]:

$$m = \underset{m}{\operatorname{argmin}} \|F \cdot C \cdot m - d\|_2^2 + \lambda_c \|D_c \cdot m\|_1 + \lambda_r \|D_r \cdot m\|_1$$

Where F is the Fourier transform operator; C is the coil sensitivity maps; D_c and D_r are the finite difference operators for the cardiac and respiratory dimensions, respectively; and λ_c and λ_r are the regularization parameters for the cardiac and respiratory dimensions, respectively.

Regularization parameters were selected empirically based on visual inspection and set to 0.005 and 0.002, respectively.

The reconstruction was implemented in MATLAB R2018a (The Mathworks, Inc, Natick, MA, USA). The Berkeley Advanced Reconstruction Toolbox (BART) was used for the ESPIRiT calibration and reconstruction [16]. Reconstructions were performed in a high-performance computing (HPC) cluster node, equipped with an 18-core Intel Xeon Gold 6140 processor and 432 GB of DDR4 memory.

2.3 Simulation Study

A simulation study was designed to investigate which step size in k_z provides optimal filling in *k*-space, while meeting the requirements that: (1) it must be small enough so as not to cause eddy current related artefacts, and (2) it must allow the calculation of a respiratory navigator as described above. Two alternative step sizes were investigated: uniform spacing (US) and tiny golden spacing (TS), which used the 7th tiny golden ratio (0.116) [26] (Figure 1). It is worth noting that the problem with eddy currents does not apply to golden angle rotations in the outer loop, due to “pairing” compensation [17]. Therefore, the golden angle was used in the outer loop.

The design of the model was similar to the one described in [15]. Ellipsoids and cylinders were used to model the heart, liver, ascending/descending aorta, left/right pulmonary arteries and the thoracic wall (Figure 3). The heart and blood vessels were given contractile dynamics, while respiratory dynamics were modelled using a craniocaudal translation. Low frequency sinusoids were used to incorporate coil sensitivities into the model. Because all these elements have analytic representations in the Fourier domain, direct simulation of the *k*-space signal is possible [17]. This prevents the so-called inverse crime bias, which arises in rasterized simulations due to the use of identical models for both data synthesis and image reconstruction.

This model was used to generate multi-channel *k*-space data for both the US and the TS reordering schemes. Simulations were repeated four times at random heart rates (drawn from a uniform distribution between 60-100 bpm) and respiratory rates (12-18 bpm) to average out possible effects due to these factors. Data were “collected” and reconstructed as described in sections 2.1 and 2.2. In addition, reference images were obtained by simulating a fully sampled stack of spirals acquisition for every cardiorespiratory state. Root mean squared error (RMSE) and structural similarity (SSIM), were calculated against these reference images to assess image quality for both reordering strategies.

2.4 Patient Study

2.4.1 Data Acquisition

Ten subjects were prospectively recruited for this study (age 21.2 ± 10.1 years). All were hospital patients for whom an MR scan had been clinically indicated. This study was approved by the local research ethics committee, and written consent was obtained from all subjects/guardians (Ref: 06/Q0508/124). A 12-channel receiver coil array (6-element body coil plus 6-element spine coil) was used and vector cardiogram time stamps were logged for retrospective cardiac gating. The proposed free-breathing whole-heart (FB-WH) cine method (see imaging protocol above) was compared with a conventional 2D multi-slice breath-hold stack in a short axis orientation (BH-SAX), with field of view = ~340 × 300 mm^2, voxel size = ~1.5 × 1.5 mm^2, slice thickness = 8.0 mm, flip angle = 70°, 10-12 slices, temporal resolution = ~40 ms. All imaging was performed on a 1.5 T MR scanner (Avanto, Siemens Healthineers AG, Erlangen, Germany).

2.4.2 Data Processing

All post processing was performed using the OsiriX open source DICOM viewing platform (OsiriX v9.0, OsiriX Foundation, Geneva, Switzerland) [27]. Prior to analysis, FB-WH volumes were reformatted into a stack of short axis cines with a slice thickness of 8 mm using the multiplanar functionality in OsiriX, in order to obtain a dataset comparable to the BH-SAX.

Image Quality Assessment. Image quality was assessed on the mid-ventricular slice of the BH-SAX data and the short axis reformatted FB-WH data. Quantitative image quality was evaluated using two objective scores: edge sharpness (ES) and contrast-to-noise ratio (CNR). The ES was calculated by drawing a line across the endocardial border, fitting a 10th order polynomial to the normalized pixel intensities (to filter out noise), and taking the maximum gradient of the fitted line as the measurement, as previously described [28]. The CNR was calculated as the ratio of the average signal difference between blood pool and myocardium to the average standard deviation in both regions [12]. The regions of interest for blood and myocardium were manually positioned in the centre of the left-ventricular cavity and the ventricular septum, respectively. In addition, subjective image quality was rated by a clinical observer on a 5-point Likert scale (0 = non-diagnostic, 1 = poor, 2 = moderate, 3 = good, 4 = excellent) in three categories: sharpness of the endocardial border, temporal fidelity of wall motion and residual artefacts.

Ventricular Volume Quantification. Quantification of left ventricular (LV) and right ventricular (RV) volumes was performed in a similar manner for each technique using in-house plugins for OsiriX by a single observer (AG, 7 years of experience in CMR). Firstly, the end-diastolic and end-systolic phases were identified for each ventricle through visual inspection of the mid-ventricular cine. The endocardial borders of all slices at end systole and diastole were then traced manually. This allowed calculation of end-diastolic volume (EDV) and end-systolic volume (ESV). Stroke volume (SV) was obtained by subtracting ESV from EDV and ejection fraction (EF) = SV/EDV × 100. The observer was presented with each anonymized volume in a random order, blinded to diagnosis, patient number and type of sequence.

2.5 Statistical Analysis

All statistical analysis was performed using R software (R Foundation for Statistical Computing, Vienna, Austria) and results were considered statistically significant if $p < 0.05$. In the simulation study, *t*-tests were used to assess the hypothesis that RMSE and SSIM values from the US and TS images have equal means. In the patient study, edge sharpness and CNR scores for the FB-WH and BH-SAX methods were compared using *t*-tests, while qualitative scores were compared using Wilcoxon signed-rank tests. Bland-Altman analysis was used to compare ventricular volume measurements between FB-WH and BH-SAX.

3 RESULTS

3.1 Simulation Study

Figure 3 shows representative axial and coronal views of the reconstructed phantom images for the US and TS sampling strategies. Visual inspection reveals better image quality in the case of US sampling, with less artefact, sharper edges and less temporal blurring. This is particularly obvious in the coronal view. The RMSE measure seems to agree with this observation (US: 0.0472 ± 0.0005 vs TS: 0.0482 ± 0.0007, $p = 0.0852$), as well as SSIM (US: 0.8937 ± 0.0217 vs TS: 0.8608 ± 0.0193, $p = 0.0954$). Since the use of TS does not seem to offer any benefits, US was used for the patient study.

3.2 Patient Study

FB-WH and BH-SAX data were acquired successfully in all patients. Acquisition time for FB-WH was 3 min 33 s, compared to 4 min 48 s ± 51 s for BH-SAX ($p < 0.05$). The average heart rate during the scans was 71 ± 13 bpm. Reconstruction time for FB-WH images was 105.6 min ± 3.3 min per patient. Representative end-systole and end-diastole images are shown in Figure 4, in a short axis orientation (multiplanar reformatted) for comparison with BH-SAX. Coronal views are shown in Figure 5 to illustrate the depiction of respiratory motion.

Subjective image quality scores were lower for FB-WH data compared to BH-SAX as shown in Table 1, but on average were still in the clinically useful range. Quantitative edge sharpness of the FB-WH images was significantly lower than the BH-SAX (0.13 ± 0.03 vs 0.64 ± 0.18 mm^{-1}, $p < 0.05$). CNR was also lower (13.8 ± 4.7 vs 16.4 ± 5.4) but this did not reach statistical significance ($p = 0.29$).

Table 2 compares the volumes obtained from the FB-WH and BH-SAX acquisitions. FB-WH slightly underestimated end diastolic volumes for both ventricles (left: −4.0 mL, −2.7%; right: −8.2 mL, −4.6%) and overestimated end systolic volumes (left: +5.3 mL, +9.3%; right: +2.6 mL, +3.7%). The remaining measures are derived from these and thus reflect the same biases. The corresponding Bland-Altman plots are shown in Figure 6.

4 DISCUSSION

This work presents a stack of spirals free-breathing whole-heart cine sequence, which leverages the golden ratio to impart incoherence to the aliasing artefacts as necessary for compressed sensing reconstruction. The main findings of this study were: (1) stack of spirals free-breathing whole-heart cine imaging was feasible in patients, (2) uniform spacing in k_z was preferable to tiny golden step spacing in *in silico* models, (3) image quality was lower than that of breath-hold short axis stacks, but was still in the clinically useful range, and (4) there was reasonable agreement between ventricular volumes measured using FB-WH and BH-SAX images. Thus, this sequence offers a rapid, easy to plan free breathing alternative to multi-slice breath-hold imaging in patients with heart disease.

The sequence used in this study is based on a previously described golden ratio stack of spirals (GRASS) sequence used for contrast enhanced angiography. The use of golden ratio steps in k_z and golden angle rotations in k_x-k_y promotes both incoherent aliasing and optimized *k*-space filling after retrospective cardio-respiratory binning. However, this sampling pattern is poorly suited to bSSFP imaging due to the large jumps in k_z, which would result in significant eddy current artefacts. Two plausible alternatives are uniform spacing and tiny golden ratio spacing, both of which have smaller step sizes, but still allow formation of a respiratory self-navigation signal. In our *in silico* model, no evidence could be found that the tiny golden ratio outperforms uniform spacing. This is slightly surprising because golden ratio spacing has been shown to outperform uniform spacing in k_z, when using spoiled gradient echo imaging [15]. The new observation may be explained by the fact that there are many more readouts (and rotations) in a bSSFP acquisition, since each readout must be kept shorter to minimize dark band artefacts. This may increase the incoherence provided by the golden angle rotations and

reduce the dependence on non-uniform sampling in k_z. Due to the better image quality in the *in silico* models, uniform spacing was used for the patient arm of the study.

In the patient study, the proposed scheme was on average 26% faster to acquire than the short axis stack. However, the short axis stack did have higher in-plane resolution, making direct comparison difficult. A more important benefit of the FB-WH technique is that it provides whole-heart coverage with isotropic resolution, enabling multiplanar reformatting (MPR) in arbitrary orientations during postprocessing. This reduces the need for multiple scans in different orientations (short axis, long axis, 4-chamber, outflow tracts, etc.), which are a time-consuming element of conventional cardiac MR protocols. An additional advantage is that FB-WH does not require breath-holding, which improves patient comfort.

The image quality of FB-WH data was lower than for BH-SAX images in terms of CNR, edge sharpness and subjective scores. There are several possible causes of lower image quality in FB-WH data. Firstly, in-plane resolution was lower in FB-WH compared to BH-SAX images, which reduces edge sharpness, as well as subjective image quality. Acquiring images with higher resolution is possible but would incur a significant cost in terms of scan and reconstruction times. Secondly, FB-WH acquisitions were highly accelerated, which makes the recovery of high-quality images challenging. Image quality could be improved by simply reducing the amount of acceleration, but this would also increase acquisition time. A better approach might be to try to improve the reconstruction itself. This could be done by using alternative sparsifying transforms [29], or incorporating low-rank constraints [30–32]. Thirdly, there was no fat suppression in our implementation of the FB-WH sequence. This is important as subcutaneous fat is a significant contributor to the aliasing artefact and increases the difficulty of reconstruction. Techniques such as fat saturation [33], alternating TR [34] or phase detection [35] can be used to attenuate signal from fat, though some would also incur an acquisition time penalty. Fourthly, spiral imaging is highly sensitive to off-resonance artefact, which manifests as blurring. It should be noted that this type of blurring increases with readout time as off-resonant spins accumulate phase. Thus, its influence is not expected to be very significant in this work, which uses a short readout time. Nevertheless, existing off-resonance correction methods [36–38] may offer some improvement. Finally, this work used a non-centred TE, i.e. $TE \neq TR/2$. This was necessary in order to maintain scanning efficiency but is suboptimal in bSSFP sequences. Using a modified trajectory, such as spiral-in/out, would enable the use of a centred TE while maintaining efficiency [39]. Aligning TE to the spin refocusing at TR/2 should improve the signal-to-noise ratio and reduce blurring due to off-resonant spins [13].

Although the FB-WH images had lower image quality than the BH-SAX data, there was still good agreement in the measurement of ventricular volumes. However, with the FB-WH technique there was a small but statistically significant underestimation of end diastolic volume and overestimation of end systolic volume, for both ventricles. This is probably due to temporal blurring and there are two possible causes. Firstly, as part of the compressed sensing reconstruction, significant amounts of temporal regularization are required to minimize the undersampling artefact. Secondly, although true temporal resolution is similar for both techniques (~40 ms), BH-SAX *k*-space data were interpolated during reconstruction to a finer temporal grid (40 reconstructed images, or about ~20 ms per frame). This is not possible with the FB-WH technique because *k*-space coordinates are continuously rotated using the golden angle.

The results reported here are consistent with other free-breathing isotropic 3D cine techniques. One study [8], using a radial koosh-ball trajectory, achieves better spatial resolution and image quality, but scan time is about four times longer than in this work. Other Cartesian techniques that offer the same spatial resolution [11,12] report more similar results in terms of image quality, agreement of ventricular volumes and scan time, but are still slower than the technique reported in this work. For the interested reader, a detailed discussion is given in Supplementary Information S1.

Finally, an important limitation of this work is the long reconstruction time and the necessary computing power. In order to enable clinical implementation, much optimization would be needed in terms of speed and memory usage, which in this work prevents the use of GPU computing. Incorporating new reconstruction technologies, such as those based on deep learning, could potentially improve the prospects in this regard.

5 CONCLUSION

In conclusion, this work presents a whole-heart imaging framework for comprehensive cardiac assessment in free-breathing conditions, with trivial planning and short acquisition time (< 4 min). While the proposed method could not provide the same image quality as a conventional multi-slice breath-hold acquisition, several factors have been identified that could mitigate this. Long reconstruction time and high computational requirements are important challenges to be addressed. Addressing these limitations, the approach may represent a promising way to simplify and accelerate the cardiac MRI workflow.

ACKNOWLEDGMENTS

We would like to express our gratitude to our clinical and research CMR radiographers in Great Ormond Street Hospital, London. This work was supported by Heart Research UK and the National Institute for Health Research (NIHR) Biomedical Research Centre at Great Ormond Street Hospital for Children National Health Service (NHS) Foundation Trust and University College London.

The authors would also like to acknowledge the use of the UCL Myriad High Performance Computing Facility (Myriad@UCL), and associated support services, in the completion of this work.

REFERENCES

[1] Judd RM. Cardiac cine imaging. Basic Princ. Cardiovasc. MRI Phys. Imaging Tech., Springer International Publishing; 2015, p. 145–59. https://doi.org/10.1007/978-3-319-22141-0_10.

[2] Jackson JI, Meyer CH, Nishimura DG, Macovski A. Selection of a convolution function for Fourier inversion using gridding (computerised tomography application). IEEE Trans Med Imaging 1991;10:473–8. https://doi.org/10.1109/42.97598.

[3] Deshmane A, Gulani V, Griswold MA, Seiberlich N. Parallel MR imaging. J Magn Reson Imaging 2012;36:55–72. https://doi.org/10.1002/jmri.23639.

[4] Lustig M, Donoho D, Pauly JM. Sparse MRI: The application of compressed sensing for rapid MR imaging. Magn Reson Med 2007;58:1182–95. https://doi.org/10.1002/mrm.21391.

[5] Jaspan ON, Fleysher R, Lipton ML. Compressed sensing MRI: A review of the clinical literature. Br J Radiol 2015;88. https://doi.org/10.1259/bjr.20150487.

[6] Piccini D, Littmann A, Nielles-Vallespin S, Zenge MO. Spiral phyllotaxis: The natural way to construct a 3D radial trajectory in MRI. Magn Reson Med 2011;66:1049–56. https://doi.org/10.1002/mrm.22898.

[7] Coppo S, Piccini D, Bonanno G, Chaptinel J, Vincenti G, Feliciano H, et al. Free-running 4D whole-heart self-navigated golden angle MRI: Initial results. Magn Reson Med 2015;74:1306–16. https://doi.org/10.1002/mrm.25523.

[8] Feng L, Coppo S, Piccini D, Yerly J, Lim RP, Masci PG, et al. 5D whole-heart sparse MRI. Magn Reson Med 2018;79:826–38. https://doi.org/10.1002/mrm.26745.

[9] Liu J, Spincemaille P, Codella NCF, Nguyen TD, Prince MR, Wang Y. Respiratory and cardiac self-gated free-breathing cardiac CINE imaging with multiecho 3D hybrid radial SSFP acquisition. Magn Reson Med 2010;63:1230–7. https://doi.org/10.1002/mrm.22306.

[10] Zhang X, Xie G, Lu N, Zhu Y, Wei Z, Su S, et al. 3D self-gated cardiac cine imaging at 3 Tesla using stack-of-stars bSSFP with tiny golden angles and compressed sensing. Magn Reson Med 2019;81:3234–44. https://doi.org/10.1002/mrm.27612.

[11] Usman M, Ruijsink B, Nazir MS, Cruz G, Prieto C. Free breathing whole-heart 3D CINE

MRI with self-gated Cartesian trajectory. Magn Reson Imaging 2017;38:129–37. https://doi.org/10.1016/J.MRI.2016.12.021.

[12] Moghari MH, Barthur A, Amaral ME, Geva T, Powell AJ. Free-breathing whole-heart 3D cine magnetic resonance imaging with prospective respiratory motion compensation. Magn Reson Med 2018;80:181–9. https://doi.org/10.1002/mrm.27021.

[13] Scheffler K, Lehnhardt S. Principles and applications of balanced SSFP techniques. Eur Radiol 2003;13:2409–18. https://doi.org/10.1007/s00330-003-1957-x.

[14] Irarrazabal P, Nishimura DG. Fast three dimensional magnetic resonance imaging. Magn Reson Med 1995;33:656–62. https://doi.org/10.1002/mrm.1910330510.

[15] Kowalik GT, Steeden JA, Atkinson D, Montalt-Tordera J, Mortensen KH, Muthurangu V. Golden ratio stack of spirals for flexible angiographic imaging: Proof of concept in congenital heart disease. Magn Reson Med 2019;81. https://doi.org/10.1002/mrm.27353.

[16] Feng L, Axel L, Chandarana H, Block KT, Sodickson DK, Otazo R. XD-GRASP: Golden-angle radial MRI with reconstruction of extra motion-state dimensions using compressed sensing. Magn Reson Med 2016;75:775–88. https://doi.org/10.1002/mrm.25665.

[17] Bieri O, Markl M, Scheffler K. Analysis and compensation of eddy currents in balanced SSFP. Magn Reson Med 2005;54:129–37. https://doi.org/10.1002/mrm.20527.

[18] Wundrak S, Paul J, Ulrici J, Hell E, Rasche V. A small surrogate for the golden angle in time-resolved radial MRI based on generalized Fibonacci sequences. IEEE Trans Med Imaging 2015;34:1262–9. https://doi.org/10.1109/TMI.2014.2382572.

[19] Pipe JG, Zwart NR. Spiral trajectory design: A flexible numerical algorithm and base analytical equations. Magn Reson Med 2014;71:278–85. https://doi.org/10.1002/mrm.24675.

[20] Winkelmann S, Schaeffter T, Koehler T, Eggers H, Doessel O. An optimal radial profile order based on the golden ratio for time-resolved MRI. IEEE Trans Med Imaging 2007;26:68–76. https://doi.org/10.1109/TMI.2006.885337.

[21] Aldefeld B, Börnert P. Effects of gradient anisotropy in MRI. Magn Reson Med 1998;39:606–14. https://doi.org/10.1002/mrm.1910390414.

[22] Bernstein MA, King KF, Zhou XJ. Handbook of MRI pulse sequences. Academic Press; 2004.

[23] Pang J, Sharif B, Fan Z, Bi X, Arsanjani R, Berman DS, et al. ECG and navigator-free four-dimensional whole-heart coronary MRA for simultaneous visualization of cardiac anatomy and function. Magn Reson Med 2014;72:1208–17. https://doi.org/doi:10.1002/mrm.25450.

[24] Huang F, Vijayakumar S, Li Y, Hertel S, Duensing GR. A software channel compression technique for faster reconstruction with many channels. Magn Reson Imaging 2008;26:133–41. https://doi.org/10.1016/J.MRI.2007.04.010.

[25] Uecker M, Lai P, Murphy MJ, Virtue P, Elad M, Pauly JM, et al. ESPIRiT—an eigenvalue approach to autocalibrating parallel MRI: Where SENSE meets GRAPPA. Magn Reson Med 2014;71:990–1001. https://doi.org/doi:10.1002/mrm.24751.

[26] Wundrak S, Paul J, Ulrici J, Hell E, Geibel M-A, Bernhardt P, et al. Golden ratio sparse MRI using tiny golden angles. Magn Reson Med 2016;75:2372–8. https://doi.org/10.1002/mrm.25831.

[27] Rosset A, Spadola L, Ratib O. OsiriX: An open-source software for navigating in multidimensional DICOM images. J Digit Imaging 2004;17:205–16. https://doi.org/10.1007/s10278-004-1014-6.

[28] Steeden JA, Atkinson D, Hansen MS, Taylor AM, Muthurangu V. Rapid flow assessment of congenital heart disease with high-spatiotemporal-resolution gated spiral phase-contrast MR imaging. Radiology 2011;260:79–87. https://doi.org/10.1148/radiol.11101844.

[29] Feng L, Benkert T, Block KT, Sodickson DK, Otazo R, Chandarana H. Compressed sensing for body MRI. J Magn Reson Imaging 2017;45:966–87. https://doi.org/10.1002/jmri.25547.

[30] Lingala SG, Hu Y, Dibella E, Jacob M. Accelerated dynamic MRI exploiting sparsity and low-rank structure: k-t SLR. IEEE Trans Med Imaging 2011;30:1042–54. https://doi.org/10.1109/TMI.2010.2100850.

[31] Otazo R, Candès E, Sodickson DK. Low-rank plus sparse matrix decomposition for accelerated dynamic MRI with separation of background and dynamic components. Magn Reson Med 2015;73:1125–36. https://doi.org/doi:10.1002/mrm.25240.

[32] He J, Liu Q, Christodoulou AG, Ma C, Lam F, Liang ZP. Accelerated high-dimensional MR imaging with sparse sampling using low-rank tensors. IEEE Trans Med Imaging 2016;35:2119–29. https://doi.org/10.1109/TMI.2016.2550204.

[33] Scheffler K, Heid O, Hennig J. Magnetization preparation during the steady state: Fat-saturated 3D TrueFISP. Magn Reson Med 2001;45:1075–80. https://doi.org/10.1002/mrm.1142.

[34] Leupold J, Hennig J, Scheffler K. Alternating repetition time balanced steady state free precession. Magn Reson Med 2006;55:557–65. https://doi.org/10.1002/mrm.20790.

[35] Hargreaves BA, Vasanawala SS, Nayak KS, Hu BS, Nishimura DG. Fat-suppressed steady-state free precession imaging using phase detection. Magn Reson Med 2003;50:210–3. https://doi.org/10.1002/mrm.10488.

[36] Noll DC, Meyer CH, Pauly JM, Nishimura DG, Macovski A. A homogeneity correction method for magnetic resonance imaging with time-varying gradients. IEEE Trans Med Imaging 1991;10:629–37. https://doi.org/10.1109/42.108599.

[37] Irarrazabal P, Meyer CH, Nishimura DG, Macovski A. Inhomogeneity correction using an estimated linear field map. Magn Reson Med 1996;35:278–82. https://doi.org/10.1002/mrm.1910350221.

[38] Chen W, Meyer CH. Fast automatic linear off-resonance correction method for spiral imaging. Magn Reson Med 2006;56:457–62. https://doi.org/10.1002/mrm.20973.

[39] Feng X, Salerno M, Kramer CM, Meyer CH. Non-Cartesian balanced steady-state free precession pulse sequences for real-time cardiac MRI. Magn Reson Med 2016;75:1546–55. https://doi.org/10.1002/mrm.25738.

CAPTIONS

Table 1. Subjective image quality scores, from 1 to 5, in all three categories. Median and interquartile range (IQR) are given for each category and each method. * indicates a statistically significant difference ($p < 0.05$).

Table 2. Ventricular volumes obtained from the BH-SAX and FB-WH acquisitions. Mean and standard deviation are given for each method, as well as bias and limits of agreement calculated using Bland-Altman analysis. Abbreviations: LV, left ventricle; RV; right ventricle; EDV, end diastolic volume; ESV, end systolic volume; SV, stroke volume; EF, ejection fraction. * indicates a statistically significant difference ($p < 0.05$).

Figure 1. Sampling strategies. Two sampling strategies were considered, both based in a nested loop strategy, with partitions in the inner loop and rotations in the outer loop. In US (uniform spacing), partition coordinates are in a Cartesian grid. In TS (tiny golden ratio spacing), partition spacing is based on the 7_{th} tiny golden ratio. In both strategies, spirals are rotated by the golden angle, θ.

Figure 2. Respiratory navigator. Head-foot projections along time, obtained using the samples along the k_z axis. Superimposed in white, the respiratory surrogate signal obtained via PCA and Fourier analysis.

Figure 3. Simulation study results. From top to bottom: fully sampled reference image, uniform step acquisition, tiny golden step acquisition. From left to right: axial, coronal views, and through time views of the numeric phantom.

Figure 4. Patient study results. Multiplanar reformation of a representative dataset in short-axis orientation and corresponding breath-hold image. Both are depicted for end diastole and end systole.

Figure 5. Patient study results. Coronal view of a representative dataset in end-inspiration and end-expiration. The white line is aligned to the dome of the right hemidiaphragm in end-inspiratory position for reference.

Figure 6. Bland-Altman plots for volumes of clinical interest: LV EDV, LV ESV, RV EDV and RV ESV. The continuous line indicates the bias and the dashed lines indicate the limits of agreement.

	Median ± IQR / 2	
	BH-SAX	**FB-WH**
Sharpness of the endocardial border	3.0 ± 0.5	2.0 ± 1.0*
Temporal fidelity of wall motion	4.0 ± 0.0	2.5 ± 0.5*
Residual artefacts	4.0 ± 0.0	3.0 ± 0.0*

	Mean ± standard deviation		Bias (limits of agreement)
	BH-SAX	FB-WH	
LVEDV (mL)	150 ± 53	146 ± 50	–4.0 (–23.6 to 15.6)
LVESV (mL)	54 ± 23	59 ± 26*	+5.3 (–4.4 to 15.0)
LVSV (mL)	96 ± 32	87 ± 26*	–9.2 (–27.2 to 8.8)
LVEF (%)	65 ± 6	61 ± 6*	–3.9 (–9.7 to 2.0)
RVEDV (mL)	177 ± 47	169 ± 48*	–8.2 (–27.2 to 10.8)
RVESV (mL)	77 ± 27	79 ± 25	+2.6 (–14.1 to 19.2)
RVSV (mL)	100 ± 23	89 ± 24*	–10.9 (–27.3 to 5.5)
RVEF (%)	57 ± 5	54 ± 3*	–4.0 (–11.9 to 4.0)

US
k_z
k_x
k_y
k_y
θ
k_x
k_z
k_x
TS
k_z
k_x
k_y
k_y
θ
k_x
k_z
k_x

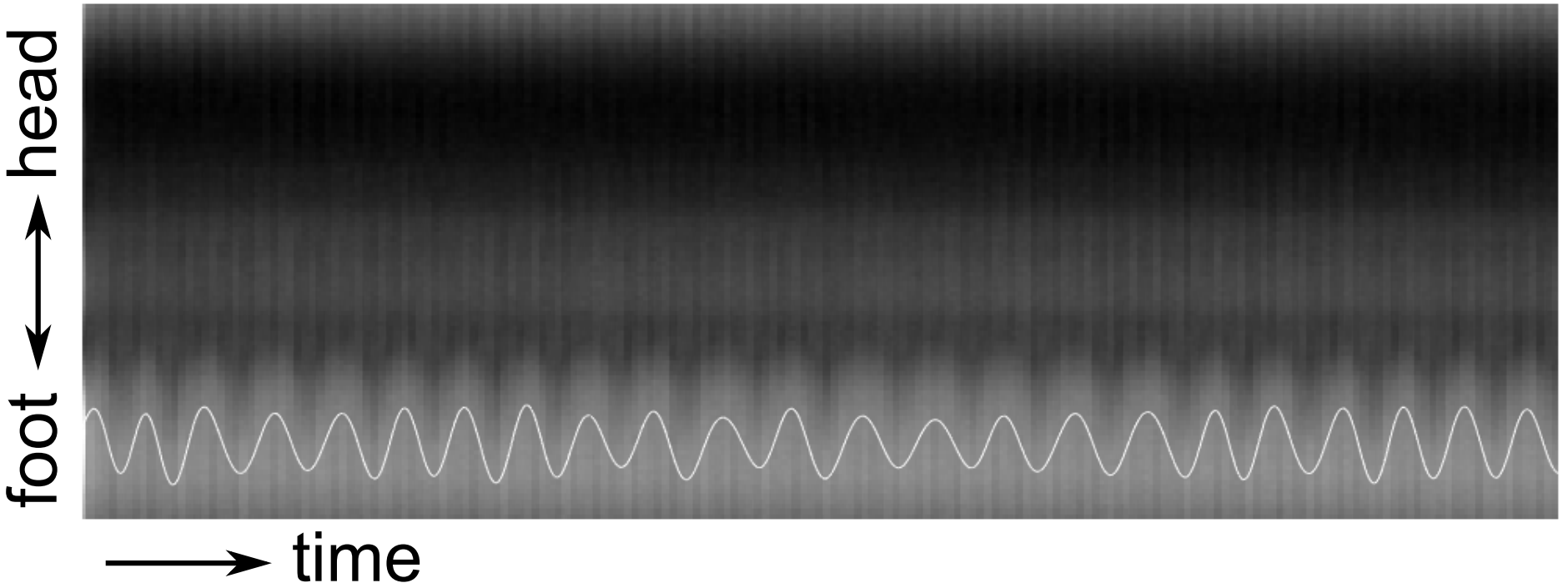
foot
head
time

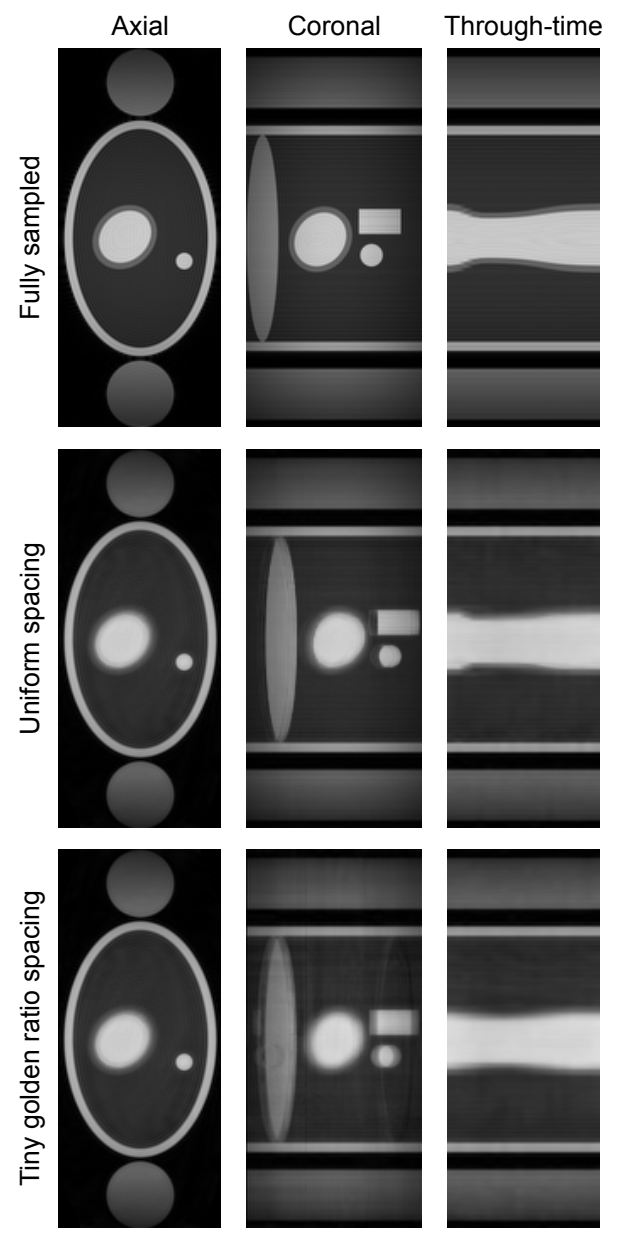
Axial
Coronal
Through-time
Fully sampled
Uniform spacing
Tiny golden ratio spacing

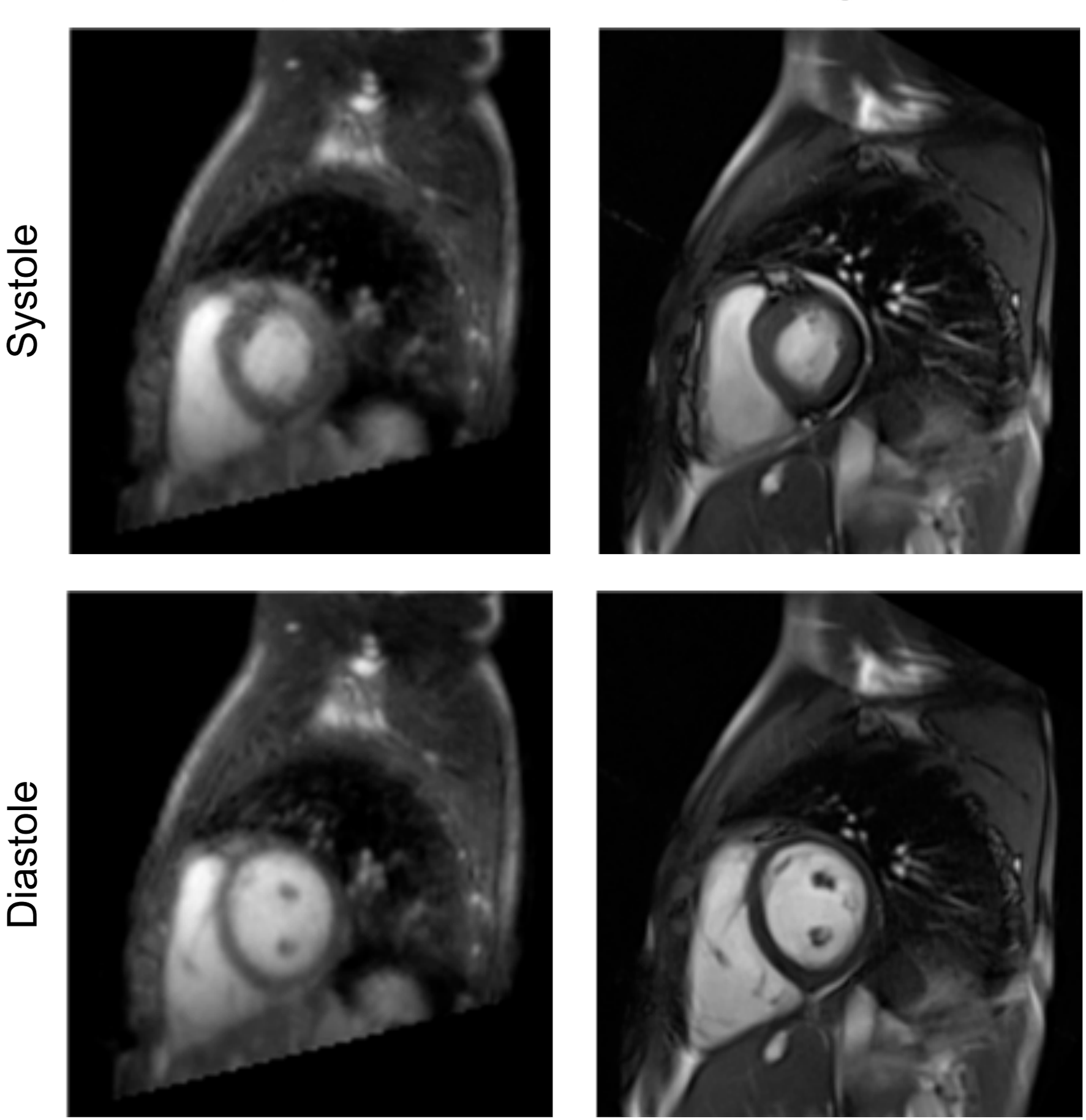
FB-WH
BH-SAX
Systole
Diastole